MINERALIZATION OF THE BAYAN OBO RARE-EARTH-ELEMENT DEPOSIT BY RECRYSTALLIZATION AND DECARBONATION

Chun-wan Wei[1], Miao Deng[1], Cheng Xu[1,2*], Anton R. Chakhmouradian[3], Martin P. Smith[4], Jindrich Kynicky[5], Wen-lei Song[6], Wei Chen[7], Bin Fu[8]

[1]Key Laboratory of Orogenic Belts and Crustal Evolution, School of Earth and Space Sciences, Peking University, Beijing 100871, China.

[2]College of Earth Sciences, Guiling University of Technology, Guiling 540001, China.

[3]Department of Geological Sciences, University of Manitoba, Winnipeg, MB R3T2N2, Canada.

[4]School of Environment and Technology, University of Brighton, Brighton BN24GJ, UK

[5]Central European Institute of Technology, Brno University of Technology, Brno 61600, Czech Republic.

[6]Department of Geology, Northwest University, Xi'an 710069, China.

[7]State Key Lab of Geological Processes and Mineral Resources, China University of Geosciences, Wuhan 430074, China.

[8]Research School of Earth Sciences, Australian National University, Canberra ACT 0200, Australia.

[*]Corresponding authors: e-mail, xucheng1999@pku.edu.cn

Abstract

The genesis of the Bayan Obo giant rare-earth-element (REE) deposit has been debated for several decades. Here, we report the isotopic effects of dynamic recrystallization in the H8 carbonatite, which is the principal ore carrier in the deposit. We studied fresh drill-core to a depth of 1.78 km and documented the elemental and C-O-Sr isotopic evolution of rock-forming dolomite during its deformation and reaction with fluids. The precursor dolomite and the products of its recrystallization differ in $\delta^{13}C_{VPDB}$ (-1.09 – 2.37‰ vs. -3.59 – 0.79‰, respectively) and $^{87}Sr/^{86}Sr$ (0.70241–0.70394 vs. 0.70288–0.71409, respectively), and show a similar $\delta^{18}O_{VSMOW}$ range (10.3 – 16.9‰). The strong negative shift in $\delta^{13}C_{VPDB}$ indicates that, locally, there was as much as 40% loss of CO_2 from the precursor dolomite, although most of the recrystallized dolomite experienced decarbonation on a smaller scale. Clumped monazite grains associated with apatite in paragenetically similar samples yielded variable in-situ Th-Pb dates (980–340 Ma), whereas those in monomineralic veinlets give a consistent age of ~400 Ma and consistent initial Nd isotopic ratios. This indicates that the wide range of dates may not represent real REE depositional events, and that the primary REE minerals deposited in the Mesoproterozoic underwent isotopic re-equilibration and REE remobilization in the Mid-Paleozoic. Recrystallization and decarbonation of dolomite in the H8 unit was facilitated by its reaction with subduction-derived silica- and halogen-rich fluid, genetically linked to plate-convergence processes along the northern margin of the North China Craton, and did not require influx of REE from an external source.

Introduction

The rare earth elements (REE = La-Lu + Y) are classified as critical metals because of their importance in renewable energy and high-technology applications (Goodenough et al., 2018). Although many minerals and rock-types contain appreciable levels of REE, minable concentrations of these elements are restricted to relatively few deposits worldwide (Chakhmouradian and Wall, 2012). China continues to dominate the global supply of REE but has been gradually reducing its production and exports because of environmental concerns (Xie et al., 2016). Consequently, there has been an increasing international effort to locate new sources of these elements. The Bayan Obo deposit is the world's largest deposit of REE ores and produces the bulk of REE exports from China (Xie et al., 2016). Dolomite rock of debatable origin (sedimentary rock vs. carbonatite; Chao et al., 1997; Xu et al., 2008) hosts most of the Bayan Obo ore body. The genesis of the REE mineralization has been hotly debated since the discovery of the deposit in 1927, including syn-sedimentary origin (Chao et al., 1997), metasomatic reworking of sedimentary carbonate rocks by carbonatitic (Smith et a., 2000; Yang et al., 2009) or subduction-derived fluids (Ling et al., 2013), and the result of carbonatite magmatism (Xu et al., 2008). New geochemical evidence supports the interpretation that the dolomite rock is of magmatic, carbonatitic origin, and that the first mineralization stage took place in the Mesoproterozoic (Song et al., 2018; Yang et al., 2019; Chen et al., 2020). Numerous lines of evidence have suggested a long history of the deposit, possibly extending from ~1300 Ma to ~400 Ma (Zhang et al., 2003; Zhu et al., 2012; Smith et al., 2015; Song et al., 2018). However, there is no consensus concerning the number of mineralization stages, with some studies suggesting as many as eleven (Chao et al., 1992). The dolomite rock shows a stratiform-like structure and evidence of strong metasomatic reworking (Smith

et al., 2015). The rocks of Bayan Obo deposit show a wide range of crustally-derived and mantle-derived radiogenic and stable isotopic compositions, and therefore the provenance and chemical composition of the post-depositional metasomatic fluids that interacted with the dolomite rock are still poorly understood. Several distinct styles of hydrothermal alteration have been recognized and occur in complexly superposed mineral assemblages containing fluorite, riebeckite, aegirine and phlogopite (Smith et al., 2007, 2015; Deng et al., 2017). The ambiguity of textural and temporal relations between the primary and alteration parageneses complicates interpretation of the REE mineralization.

Carbonatites are known to contain the highest concentrations of REE ($n \times 10^{2\text{-}4}$ ppm) of any igneous rock and are considered to be an exploration target of major importance. Although there are more than 500 known carbonatites in the world, currently only a few are being mined for the REE, e.g., Bayan Obo, Maoniuping and Dalucao, Muluozhai deposits in China, Mountain Pass in the USA, and Mount Weld in Australia (Weng et al., 2015; Smith et al., 2016; Verplanck et al., 2016). The key question that needs to be addressed is how the Bayan Obo dolomite carbonatite became the host for a giant REE deposit, dwarfing in size the REE deposits hosted by carbonatites elsewhere.

Here, we report in-situ geochemical analyses for C and O stable isotopes and Sr and Nd radioisotopes on precursor and recrystallized dolomite grains and REE minerals. The samples were obtained from the dolomite host rock, recovered as part of a 1776-m long drill-core. The C, O and Sr isotope compositions of recrystallized dolomite provide new constraints on the nature of metasomatic fluids and mineralization processes at Bayan Obo. A combination of in-situ dating and Nd isotope analyses of REE minerals provides a clear record of two mineralization stages, in

which the REE grade of the Mesoproterozoic carbonatites was enhanced by recrystallization and CO_2 degassing at ~400 Ma.

Geological Background

The Bayan Obo REE deposit is located on the northern margin of the North China Craton (NCC), bordered by the Bainaimiao arc to the north (Fig. 1). The basement rocks in this region consists of Archean–Paleoproterozoic metamorphic rocks that are unconformably overlain by a ~8.5 km thick strata sequence of the Mesoproterozoic Bayan Obo Group. These sediments were deposited within the Bayan Obo marginal rift during the Mesoproterozoic continental breakup of the NCC (Zhang et al., 2017). The Mesoproterozoic rifting was accompanied by the emplacement of basalts, basaltic trachyandesites and carbonatite dykes (Yang et al., 2011). The Bayan Obo Group comprises 18 lithological units (H1-H18), including metasandstones, limestones, slates, dolomite rocks and metavolcanics. The H1-H9 units in ascending order from base to top are composed of the main part of the outcrops in the Bayan Obo area (Bai and Yuan, 1985). Chao et al. (1997) classified the H1-H8 units as meta-sedimentary rocks, whereas a recent study shows that the H2 unit is of magmatic origin, supported by the presence of melt inclusions in quartz (Xie et al., 2020). The REE-Fe orebodies are hosted in the H8 dolomite, and the H9 slate unit is the dominant wall-rock for the Bayan Obo orebodies (Zhang et al., 2003). The H9 unit has been divided into four sub-types: biotite type, calcite-biotite type, calcite type, and K-feldspar type according to their mineral assemblages. Xie et al. (2020) suggested that the calcite-biotite type is of a carbonatite affinity, as the mineral assemblage and texture is similar to a biotite-rich calcite carbonatite. Near the ore deposit, a few dozen Mesoproterozoic

carbonatite dykes, composed mainly of dolomite, calcite and rare Sr, Ba and REE carbonates, intruded the Bayan Obo Group low-grade metasediments and basement rocks, which were fenitized along the contact (Le Bas et al., 2007). Based on their mineralogical composition, the dykes were classified as dolomite, dolomite-calcite and calcite carbonatites (Wang et al., 2002). Late Paleozoic Hercynian dioritic-granitic plutons were emplaced to the southeast of the deposit, including quartz monzonite, monzonitic granite and biotite granite (Zhang et al., 2003; Ling et al., 2014).

The H8 unit extends sub-latitudinally over a distance of 18 km, has a maximum width of 3 km and in plan view, is represented by a spindle-shaped stratified body. Rare xenoliths of mafic metamorphic rock have been found in the H8 carbonatites (Appendix Fig. A1A). The unit comprises texturally variable (inequigranular, fine- to coarse-grained, massive to foliated) dolomite, with subordinate riebeckite, phlogopite, fluorite, fluorapatite, magnetite, and REE minerals (Appendix Fig. A1B-D). The mineral assemblages of dolomite rocks are rather variable. According to the mineral occurrences, the proportions of riebeckite and phlogopite vary from 1 to 20 vol.%, and the fluorite content ranges from 1 to 20 vol.%. The H8 rocks underwent extensive deformation and metasomatic reworking, and mainly contain three types of ores (disseminated, banded and massive). The REE contents range from <3 wt.%, 3 to 6 wt.%, and 6 to 12 wt.% REE_2O_3 for massive, disseminated and banded ores, respectively (Xu et al., 2008). The studied drill-core was extracted from the East orebody, and shows significant variations in total light REE (LREE = La-Sm) content ranging from 1- 6 wt.% (Song et al., 2018).

Methods

The major-element compositions of dolomite crystals in the drill-core were analyzed

using a JXA-8100 electron microprobe (EMP) at Peking University. The operating conditions were a 15 kV accelerating voltage and a beam-current of 10 nA, with an electron beam defocused to 10 μm. A set of appropriate matrix-specific standards and optimal instrumental conditions (detector type, beam settings and counting statistics) were carefully chosen by performing multiple measurements. All raw data were corrected using a ZAF (Z, atomic number; A, absorption; F, fluorescence) procedure.

In-situ laser-ablation inductively-coupled-plasma mass-spectrometry (LA-ICP-MS) at Peking University was used to measure the abundances of selected trace elements in the dolomite, with an Agilent 7500Ce mass spectrometer coupled to a 193-nm ArF excimer laser. The diameter of the ablation spot ranged between 40 and 60 μm depending on the size of the individual mineral grains. The measurements were done at a laser energy density of 5.5 J/cm^2 and a repetition rate of 5 Hz. Standard NIST610 glass was used for external calibration, and the CaO content of the same minerals determined independently by EMP analysis was used as an internal standard. The analytical uncertainty for most trace element concentrations was within 5% based on repeated analyses of standards NIST 612 and NIST 614.

In-situ Th-Pb dating of monazite and bastnäsite in polished thin section was carried out using quadropole ICP-MS (Agilent 7700×) with a Laser-ablation system (ASI RESOnetics S-155, 193 wavelength) at Nanjing FocuMS Technology Co. Ltd. Analyses were performed with a beam diameter of 24 μm and a repetition rate of 6 Hz. The initial conditions were set at $ThO^+/Th^+ < 0.3\%$ to minimize the production of molecular compounds. Each analysis consisted of an approximately 20-s background acquisition and a 65-s sample acquisition. The monazite standard 44069 (424 ± 1 Ma, Aleinikoff et al., 2006) and bastnäsite standard K-9 (118±1 Ma, Sal'nikova et al., 2010) were used as the external standards to monitor the instrumental shift and the laser-

induced U-Th-Pb fractionation. Off-line data selection and integration were performed by using ICPMSDataCal software, and age calculations were processed using the ISOPLOT program (Ludwing, 1994). The uncertainties associated with the age determinations are quoted at 1σ and ages were calculated at the 95% confidence level. Additional details of the analytical procedure are presented in Yang et al. (2014).

After electron microprobe analysis and SEM-BSE imaging, small pieces of polished thin sections of dolomite samples were cut and mounted in Buehler EpoFix epoxy resin, together with carbonate reference materials: Hammerfall dolomite, UW6220 dolomite and GTS144 ankerite. In-situ C and O isotope analyses of carbonates were carried out using an ion microprobe SHRIMP-SI (Sensitive High Resolution Ion Microprobe for Stable Isotopes) in the Research School of Earth Sciences, Australian National University. The analytical conditions were similar to those outlined in detail by Hu et al. (2018). Analyses of the standards were typically performed after every three to five unknowns to correct for instrumental mass-dependent fractionation. A 10 kV, 2 nA primary beam of $^{133}Cs^{+}$ ion was focused to a ~ 6 μm diameter on the sample surface. Negative ions of $^{12}C^{-}$, $^{13}C^{-}$, $^{16}O^{-}$ and $^{18}O^{-}$ were measured with Faraday cups. All the data for the unknowns were calibrated initially against Hammerfall dolomite ($\delta^{13}C_{VPDB}$ = -0.28±0.07 ‰, and $\delta^{18}O_{VSMOW}$ = 21.43±0.02 ‰, 2σ; Hu et al., 2018) and further corrected for matrix effects, using a method similar to that of Śliwiński et al. (2016a, b). Plots of in-situ C isotope ratios versus Fe contents of the dolomite from different paragenetic settings do not obviously show correlation (Appendix Fig. A2). The corrected $^{18}O/^{16}O$ ratios are reported in standard $\delta^{18}O$ notation, relative to Standard Mean Ocean Water (SMOW) and the $^{13}C/^{12}C$ ratios are reported relative to Vienna Pee Dee Belemnite (VPDB).

The in-situ Nd isotopic compositions of monazite and bastnäsite in thin section

were measured by multi-collector (MC) ICP-MS using a Thermo-Finnigan Neptune instrument coupled to a 193-nm ArF excimer laser-ablation system at the Institute of Geology and Geophysics, Chinese Academy of Sciences. Prior to analysis, the Neptune MC-ICP-MS was tuned and optimized for maximum sensitivity using JNdi-1 standard solution. The diameter of the laser spot and frequency were adjusted to between 20-24 μm and 4-10 Hz, respectively, depending on the Nd concentration and size of individual mineral grains in the thin sections. Each spot analysis incorporated an approximately 60-s signal acquisition. The $^{147}Sm/^{149}Sm$ and $^{147}Sm/^{144}Sm$ values were used to calculate Sm mass bias and ^{144}Sm composition, respectively (Yang et al., 2008). The $^{146}Nd/^{144}Nd$ ratio was used as interference correction for ^{144}Sm. Normalized $^{143}Nd/^{144}Nd$ and $^{147}Sm/^{144}Nd$ isotopic ratios were calculated using the exponential law (Depaolo and Wasserburg, 1976). The $^{147}Sm/^{144}Nd$ ratio was then further calibrated externally against the $^{147}Sm/^{144}Nd$ ratio of monazite standards, Jeffson and Nama (Liu et al., 2012), during the analytical sessions. The average measured $^{143}Nd/^{144}Nd$ of Nama is 0.511886±22 (2σ, n=22) and $^{143}Nd/^{144}Nd$ of Jeffson is 0513087±24 (2σ, n=9), which are consistent with the recommended values [$^{143}Nd/^{144}Nd$= 0.511896±32 (2σ; Nama); $^{143}Nd/^{144}Nd$ = 0.513057±93 (2σ; Jeffson); Liu et al., 2012]. More detailed information on the in-situ Nd isotopic analysis employed in the present work is available in Yang et al. (2008).

In-situ Sr isotopic compositions of dolomite were measured using a RESOlution laser ablation system coupled to a Nu Plasma II MC-ICP-MS at the State Key Laboratory of Geological Processes and Mineral Resources, China University of Geosciences (Wuhan). The analyses of dolomite grains were carried out using a spot size of 50 -75 μm with a repetition rate of 10 Hz and an energy density of 4-5 J/cm^2. The isotopic ratios were quantified in a static multi-collector mode at low resolution,

using seven Faraday collectors and a mass configuration array from ^{82}Kr to ^{88}Sr to monitor variations in Kr, Rb and Sr signals. An in-lab coral standard was analyzed as the external standard. The average $^{87}Sr/^{86}Sr$ isotopic composition obtained for the coral standard is 0.70920±8 (2σ, n=20), which corresponds to the recommended value of 0.70923±4 (2σ) (Pu et al., 2005). The analytical procedure and data-reduction strategy are described in more detail in Tong et al. (2015).

The C-O isotopic compositions of dolomite in drill-core were measured at the Institute of Geochemistry, Chinese Academy of Science, using an Isoprime continuous-flow isotope-ratio mass-spectrometer (Elementar). The results are reported in conventional delta notation, as per mil (‰) variation relative to the VPDB and SMOW for carbon and oxygen, respectively. The Sr and Nd isotopic compositions of the whole-rocks were analyzed in solution using a VG AXIOM MC-ICP-MS instrument at Peking University. Mass fractionation corrections for the Sr and Nd isotopic ratios were normalized to an $^{86}Sr/^{88}Sr$ ratio of 0.1194 and a $^{146}Nd/^{144}Nd$ ratio of 0.7219, respectively. Repeated measurements of standards NBS987 and JNdi yielded an average $^{87}Sr/^{86}Sr$ value of 0.710254±14 (2σ, n=6) and $^{143}Nd/^{144}Nd$ value of 0.512094±34 (2σ, n=6), respectively, consistent with the recommended values of 0.710248 (NBS97) and 0.512113 (JNdi), respectively. To calculate the initial Sr-Nd isotopic values, the Rb, Sr, Sm and Nd concentrations of whole-rock samples were measured by in solution by ICPMS (Thermo Fisher Scientific X-Series II). Repeated analyses of well-characterized standards indicate that the accuracy of trace element measurements was better than 10%.

Results

Sample selection and petrography

Core from depths of 200 to 1776 m in drill hole #WK15-05 was collected for petrographic observation and geochemical analyses (Appendix Fig. A3A, B). The sample interval in the core was ~20 m for thin-sections and 50 m for whole-rock analyses, respectively. The examined drill-core samples are composed of large amounts of fine-grained and minor coarse-grained dolomite rocks. Some fine-grained dolomite rocks contain relatively large dolomite porphyroclasts (0.4-3.4 × 0.3-1.8 mm in size) with serrated margins immersed in a fine-grained (0.01-0.03 mm across) dolomite matrix (Fig. 2A, B; Appendix Fig. A3C). The porphyroclasts represent residual of precursor dolomite after deformation and hydrothermal reworking. The matrix grains are interpreted to be the products of dynamic recrystallization, as shown by the polygonal shapes and triple grain junctions of the crystals (Fig. 2C, D, and Appendix Fig. A3D), and indicated by the locally developed preferred orientation (Appendix Fig. A3D). Under CL (cathode-luminescence), the dolomite porphyroclasts display weak red-luminescent rims and non-luminescent cores (Fig. 2B), whereas the recrystallized, fine-grained dolomite, which is associated with fluorite and REE minerals is non-luminescent (Fig. 2D). Some red-luminescent dolomite rims are surrounded by bright-orange rims, which implies two stages of dolomite growth (Fig. 2E, F).

Monazite and bastnäsite Th-Pb geochronology

Monazite (ideally, $LREEPO_4$) is a common REE mineral in the studied samples. It normally occurs as clusters of minute crystals associated with apatite, which is probably a precursor phosphate phase (Fig. 3A), as well as disseminated grain clusters and in veinlets containing REE fluorcarbonates (particularly, bastnäsite $LREECO_3F$) and fluorite; monomineralic veinlets of monazite were also observed (Fig. 3B). The Th-Pb ages of monazite and bastnäsite from paragenetically different settings

were measured in-situ (i.e., in polished thin sections) in H8 unit samples from the 1482–1769 m depth interval (Appendix Table A1). When combined with the previously reported Sm-Nd isochron dates of whole-rock and REE mineral samples, the data cover a wide range, with two strong peaks at ~1.3 Ga and ~400 Ma (Fig. 4). Anchimonomineralic monazite veinlets yielded a much more restricted range of dates clustering around 400 Ma (Fig. 3B), in comparison with monazite grains intergrown with bastnäsite and apatite (~340-980 Ma, Fig. 3A). The in-situ Th-Pb age analyses were performed on disseminated anhedral (50-200 μm) and large (up to 0.8 cm in length) bastnäsite grains. Their ages cluster at ~420 Ma (Fig. 4).

Major and trace element geochemistry

The precursor and recrystallized dolomite varieties can be clearly distinguished on the basis of their chemical compositions (Appendix Tables A2, A3). The recrystallized variety has higher Fe and Mn contents relative to the porphyroclasts. Their compositions form two partially overlapping fields, consistent with chemical re-equilibration of the porphyroclasts during recrystallization (Fig. 5A, B). Both varieties contain elevated Sr abundances (~2550 and ~2070 ppm, respectively), which are similar to Sr levels in carbonatitic dolomite (Chakhmouradian et al., 2016) and higher than the sedimentary carbonate rocks in the Bayan Obo area (<200 ppm; Zhang et al., 2003). The porphyroclast and recrystallized dolomite show similar average chondrite-normalized (CN) REE profiles (Fig. 6). The profiles of dolomite porphyroclasts are smooth and exhibit a slight negative slope (La/Yb_{CN} = 2–15). The recrystallized variety yields either negatively or positively sloping profiles (La/Yb_{CN} = 0.2–15) that overlap with those of porphyroclasts. The LREE contents of porphyroclastic and recrystallized dolomite are similar (e.g., La = 2.5–21 ppm vs. 0.6–27 ppm, respectively), whereas

many recrystallized grains exhibit a small positive Eu anomaly (Eu/Eu* = 1.1–2.5). Lower La/Nd_{CN} and La/Ho ratios, compared to the precursor dolomite, have been determined in many of the recrystallized grains (Fig. 5C, D), but their Y/Ho ratios are indistinguishable. The absence of any departure of the Y/Ho ratio from typical carbonatitic values (Chakhmouradian et al., 2016) at extremely variable La/Ho values suggests LREE mineral deposition during dolomite recrystallization (Bau and Dulski, 1995).

C-O stable isotope compositions

In-situ oxygen isotope analyses of the precursor and recrystallized dolomite yielded a similar range of values: $\delta^{18}O_{VSMOW}$ = 10.3–16.9 ‰, whereas the carbon isotopic values vary significantly (Appendix Table A4). The porphyroclasts are generally enriched in heavy C relative to the recrystallized dolomite ($\delta^{13}C_{VPDB}$ = -1.09 – 2.37 ‰ vs. -3.59 – 0.79 ‰, respectively). The drill-core samples give a similar range of $\delta^{18}O_{VSMOW}$ values (12.0–15.3 ‰) in comparison to the in-situ analyses, but a more limited range of $\delta^{13}C_{VPDB}$ ratios (-2.3–0.4 ‰), which overlaps with both precursor and recrystallized dolomite compositions (Appendix Table A5). The dolomite samples are distinct from both mantle-derived carbonatites and metasedimentary dolomite of the Bayan Obo Group in terms of their C-O isotopic signature (Fig. 7A).

Sr and Nd isotope compositions

In-situ Sr isotopic analyses of the dolomite also show a large variation (Appendix Table A6). The porphyroclasts are characterized by low $^{87}Sr/^{86}Sr$ ratios (0.70241–0.70394), which increase slightly towards their rim. The Sr isotopic ratios of the recrystallized variety show some overlap with the precursor values but are generally higher and far

more variable (0.70288–0.71409). A similar, albeit more limited, range of values was recorded for drill-core samples (0.70288-0.70533; Appendix Table A7). The high Sr content and low Rb/Sr ratio of the Bayan Obo dolomite imply that the present-day $^{87}Sr/^{86}Sr$ ratios accurately reflect the composition of its source and were only negligibly affected by ^{87}Rb decay. In an $^{87}Sr/^{86}Sr$ vs. $\delta^{13}C_{VPDB}$ plot, the two dolomite varieties form two compositional fields with relatively little overlap (Fig. 7B).

The Nd isotopic ratios were measured independently for the same monazite and bastnäsite grains, and used to calculate the initial $^{143}Nd/^{144}Nd_{(t)}$ ratios (Appendix Table A8). The REE phases gave broadly similar $T_{CHUR}(Nd)$ model ages ranging from 1.20 to 1.35 Ga, which imply a common LREE source. Combined with the initial Nd isotopic ratios of drill-core samples, calculated for the peak ages of 1300 and 400 Ma, the measured REE mineral ages and $\varepsilon Nd_{(t)}$ values show a robust linear correlation (Fig. 8).

Discussion

Origin of metasomatic fluids

The precursor porphyroclastic dolomite is characterized by low $^{87}Sr/^{86}Sr$ ratios, which are consistent with a mantle origin and similar to those of the Mesoproterozoic carbonatite dykes uncontaminated by wall-rock feldspathic material (Le Bas et al., 2007). However, this dolomite is characterized by higher $\delta^{13}C_{VPDB}$ values relative to those typically observed in mantle rocks (-7 to -5 ‰; Ray et al., 1999), implying that its source was enriched in ^{13}C (or depleted in ^{12}C). The possible mechanisms that could cause such enrichment in mantle-derived melts or fluids are fractional crystallization, assimilation of sediments, or addition of subducted crustal materials to the mantle C reservoir (Xu et al., 2014). Fractional crystallization and sediment

contamination can be ruled out, as these processes generate concomitant enrichment in ^{13}C and ^{18}O (Ray and Ramesh, 2000), which is not observed (Fig. 7A). The enrichment of ^{13}C by the incorporation of recycled oceanic carbonates ($\delta^{13}C_{VPDB} \approx 0$ ‰; Veizer et al., 1992) into the mantle source region remains a possibility. Paleotectonic reconstructions demonstrate that between 2.3 and 1.9 Ga, the northern edge of the NCC was an active continental margin characterized by southward subduction (in present-day coordinates) and Andean-type magmatism, which culminated with the amalgamation of the NCC with the Columbia supercontinent by ~1.8 Ga (Kusky et al., 2016). Multiple manifestations of arc magmatism SE of Bayan Obo (Yang and Santosh, 2015), and the presence of high-pressure eclogite xenoliths derived from a recycled slab in Paleoproterozoic carbonatites ~300 km further inland (Xu et al., 2018), provide unambiguous evidence that subducted material was present in the mantle beneath this part of the NCC. Subduction processes could have played a key role in REE enrichment of the mantle sources of the Bayan Obo carbonatites (Xu et al., 2014; Hou et al., 2015).

The recrystallized dolomite is indistinguishable from the porphyroclasts in its O isotopic signature but is characterized by lower $\delta^{13}C_{VPDB}$ and higher $^{87}Sr/^{86}Sr$ values (Fig. 7B). Their $\delta^{18}O_{VSMOW}$ values are significantly higher than the primary mantle-derived carbonatite (Taylor et al., 1967). The negative shift in $\delta^{13}C_{VPDB}$ values in the recrystallized dolomite is probably a reflection of isotope fractionation due to degassing (Suwa et al., 1975; Valley, 1986, Demeny et al., 1994). It is well known that the Bayan Obo dolomite rock underwent strong metasomatism (Smith et al., 2007, 2015; Deng et al., 2017); hence, the observed changes in $\delta^{13}C_{VPDB}$ must be discussed in the context of metasomatic reworking.

Three possible scenarios should be considered for the origin of the metasomatic

fluids responsible for the chemical and isotopic re-equilibration of the precursor dolomite. (1) mantle-derived fluids are typically enriched in ^{12}C and depleted in ^{87}Sr relative to fluids of crustal provenance. Archean-Paleoproterozoic and Mesozoic mantle peridotite xenoliths from the NCC show the sub-continental lithospheric mantle is characterised by relatively low Sr isotopic compositions (0.7030-0.7060; Zhang et al., 2020; Zou et al., 2020). Thus, a mantle origin for the fluids can probably be ruled out based on the high levels of radiogenic Sr in the recrystallized samples (Fig. 7B). (2) Granite-derived fluids could, in principle, cause the observed shift in $^{87}Sr/^{86}Sr$ ratios, but are not likely to reset the C isotopic ratio because CO_2 solubility in non-arc silicic-rich melts is very low (Lowenstern, 2001). More importantly, the Bayan Obo granitoids were emplaced during the late Permian (Zhang et al., 2003), i.e., they are younger than the bulk of the REE mineralization (Fig. 4). The older (Silurian-Devonian) granitoids, which intruded the northern margin of the NCC, on the other hand, have relatively low $^{87}Sr/^{86}Sr$ ratios (~0.706, Fig 7B; Zhang et al., 2014), i.e., they cannot explain the extremely radiogenic signature of some of the recrystallized dolomite (Fig. 7B). Considering the abundance of silicate minerals in the H8 unit and the low values of the partition coefficients for Sr between fluids and silicate (or carbonate) melts (Song et al., 2016), the high Sr content and initial $^{87}Sr/^{86}Sr$ ratio recorded in the recrystallized dolomite would have required massive fluid infiltration relative to the precursor rocks. (3) Subduction-zone processes are commonly proposed as an alternative source of the fluids responsible for the reworking of the H8 unit (Ling et al., 2013). The northernmost margin of the NCC is delineated by the Solonker suture, along which the Paleo-Asian Ocean closed to form the southern sections of the Central Asian orogenic belt (Fig. 1). The suture initially developed during the accretion of the Bainaimiao arc onto the passive margin of the NCC at 437–453 Ma (Eizenhöfer and Zhao, 2018).

Subduction-zone fluids are dominated by aqueous alkali and aluminosilicate components and characterized by elevated Sr and Cl levels (Manning, 2004). With increasing hydration and proximity to metasedimentary rocks at the top of the subducted slab, an aqueous (Sr, Cl, Si)-bearing fluid would have a radiogenic $^{87}Sr/^{86}Sr$ signature consistent with our data (Scott et al., 2019, Fig. 7B). Furthermore, fluid-inclusion studies indicate that the ore-forming fluids involved in the development of the Bayan Obo REE mineralization mostly have compositions in the H_2O–CO_2–NaCl system (Smith and Henderson, 2000).

Rayleigh fractionation during degassing

Here, we propose that the H8 dolomite carbonatite underwent textural, trace-element and isotopic re-equilibration with an externally derived fluid, which caused the observed C-Sr isotope decoupling. The negative shift in $\delta^{13}C_{VPDB}$ and precipitation of alkali silicates (phlogopite, riebeckite) and fluorite can be modeled as Rayleigh devolatilization involving a fluid capable of mobilizing fluorine and silicon from the subduction zone:

$$3Ca(Mg,Fe)(CO_3)_2 + 3SiO_3^{2-} + Al^{3+} + K^+ + 2HF + 8H^+ = 3Ca^{2+} + K(Mg,Fe)_3[Al(Si_3O_{10})]F_2 + 5H_2O + 6CO_2 \quad (1)$$

$$5Ca(Mg,Fe)(CO_3)_2 + 8SiO_3^{2-} + 2Na^+ + 24H^+ + 0.5O_2 = 5Ca^{2+} + Na_2(Mg,Fe^{2+})_3Fe^{3+}{}_2Si_8O_{22}(OH)_2 + 11H_2O + 10CO_2 \quad (2)$$

$$Ca(Mg,Fe)(CO_3)_2 + 2HF + 2H^+ = CaF_2 + 2H_2O + (Mg,Fe)^{2+} + 2CO_2 \quad (3)$$

This formulation provides useful constraints on isotope fractionation in natural systems (Valley, 1986): $\delta f = 1000 \times (F^{\alpha-1} - 1) + \delta i$, where F is the C or O fraction remaining in the rock after the above reaction, α is the CO_2–dolomite fractionation factor, and δi and δf are the initial and final isotopic values of the dolomite, respectively.

We used fractionation factors for C and O determined experimentally (Chacko et al., 1991), and assumed that the H8 dolomite re-equilibrated at T = 400–500 °C, because of the homogenization temperature of fluid inclusions trapped during the main REE depositional stage at Bayan Obo >400 °C (Smith and Henderson, 2000; Weng et al., 2015). The initial $\delta^{13}C_{VPDB}$ (0.72 ‰) and $\delta^{18}O_{VSMOW}$ (13.51 ‰) values were used as the average C-O isotope values of the precursor dolomite porphyroclasts. Using the average $\delta^{13}C_{VPDB}$ ratio of recrystallized dolomite (-1.33 ‰) as the final carbon isotopic composition, the F(carbon) value was calculated to be ~0.58 (Fig. 7A), i.e., approximately 42 % of C was released as CO_2 from the H8 unit during its metasomatic reworking. If we consider that the contribution of organic C ($\delta^{13}C_{VPDB} \approx -25$ ‰) to the subducted fluid was 0.24 % (Plank and Manning, 2019), ~40 % of the Bayan Obo dolomite was degassed (Appendix Fig. A4). Typical subduction-zone fluids contain low CO_2 (Manning, 2004), and organic carbon (CH_4) was found only in trace amounts in fluid inclusions from mineralized parageneses (Smith and Henderson, 2000). Therefore, the negative shift of carbon in Bayan Obo dolomite is not likely to be caused by organic carbon in subduction-derived fluids. Degassing reactions normally lower the $\delta^{18}O_{VSMOW}$ value of re-equilibrated carbonate minerals by no more than 3 ‰ because of the calc-silicate limit (F> 0.6) even at high levels of decarbonation (Valley, 1986). However, ^{18}O is partitioned preferentially into carbonates relative to their associated silicate phases (Chacko et al., 2001), and fluids derived from subducted metasediment-dominated rocks show enrichment in ^{18}O ($\delta^{18}O_{VSMOW} \geq 9.6$ ‰; Scott et al., 2019). Thus, dolomite recrystallization involving such fluids is not expected to have a significant effect on the primary O isotopic signature. A similar example of the degassing of carbonate minerals with little O isotope depletion has been reported by Wei et al. (2020).

Decarbonation during metasomatic reworking will result in volume loss. Volume loss occurred in response to negative specific-volume changes during decarbonation reactions (1, 2 and 3), and was accompanied by the closure of reaction-induced porosity by creep, grain-boundary sliding and pressure solution as fluid overpressures dissipated (Balashov et al., 1998). These processes are manifested by the zones of recrystallized dolomite and the formation of fluorite and monazite-apatite segregations, stringers and schlieren in the H8 unit. The volume change due to decarbonation can be semi-quantitatively estimated given that the precursor rock was effectively composed of monomineralic dolomite. If Rayleigh volatilization follows a normal calc-silicate decarbonation trend as Reactions (1 and 2), the approximate volume change in the precursor rock would be ~ +6 % when F(carbon) ~0.6. However, Reactions (1 and 2) are constructed on the basis of conserved Fe and Mg, which is unlikely in an aqueous-chloride solution, so this volume expansion is unlikely to be realistic (Yardley, 2005). Using SUPRCRT92 to calculate molar volume changes on reaction, and assuming a Rayleigh devolatilization parameter of ~0.6 (i.e., 40 mol% $Ca(Mg,Fe)(CO_3)_2$ loss), fluorite formation via Reaction (3) would result in a rock volume change of ~ -25 % at P = 1 kbar and T = 25-450 ˚C (Johnson et al., 1992). It is clear that Reactions (1), (2) and (3) operated in combination, and the Mg and Fe released during dolomite dissociation were incorporated in ferromagnesian silicates, both in the H8 unit and in the adjacent fenites (Smith, 2007). According to the fluorite and silicate minerals compositions of the H8 dolomite carbonatite, and the total volume change of decarbonation reactions would be ~ -10 % when F(carbon) ~ 0.6. The corresponding release of CO_2 as a fluid was recorded in the chemistry of the fluid inclusions (Smith and Henderson, 2000).

The Nd isotopic data suggest a two-stage evolutionary history, involving the

476 separation of a LREE-bearing carbonatite magma from the mantle at ~1.3 Ga, and
477 subsequent periodic remobilization of the REE until ~400 Ma (Fig. 8). There is no
478 isotopic evidence to suggest any significant influx of LREE from external sources, such
479 as the Paleozoic granitoids. However the late-stage metasomatic hydrothermal
480 reworking played a significant role in the REE re-enrichment of the Bayan Obo
481 deposits.

482 The decarbonation process mentioned above would have led to the decomposition
483 of the precursor dolomite and precipitation of the recrystallized dolomite, fluorite, and
484 silicate minerals. The precursor and recrystallized dolomite display similar chondrite
485 normalized REE profiles and relatively consistent near-chondritic Y/Ho ratios (Fig. 5
486 and Fig. 6), suggesting that the decomposition of dolomite resulted in the enrichment
487 of REE that are readily immobilized in such low-solubility phases as monazite (Van
488 Hoozen et al., 2020). Therefore, the decarbonation process caused REE enrichment
489 of the residual dolomite body with these elements.

490

491 *REE mineralization timing*

492 Two questions pivotal to the discussion of the Bayan Obo deposit are when and why
493 such extensive recrystallization of the H8 dolomite took place. The published Sm-Nd
494 isochron ages of whole-rock and mineral samples, and Th-Pb ages of monazite and
495 bastnäsite cover a wide range from 1400 to 300 Ma (Fig. 4). It is now widely accepted
496 that REE minerals were deposited at Bayan Obo over a period of at least 1 billion
497 years (Song et al., 2018). In this study, the in-situ dating of monazite associated with
498 apatite in paragenetically similar samples gave a wide range of dates, from ~340 to
499 980 Ma, whereas monomineralic monazite veinlets are characterized by relatively
500 consistent isotopic characteristics and an age of ~400 Ma. This discrepancy indicates

that the 1300–400 Ma date range may not represent the REE depositional ages. The older dates could arise from variable degrees of Pb loss during dolomite reaction with a fluid and recrystallization. The monazite was affected by a thermal event at ~400 Ma, which resulted in isotopic re-equilibration and resetting of the Th-Pb system. The tectonic evolution of the Bayan Obo area is inferred to have involved regional metamorphism during two major lithospheric events: crustal extension and rifting in the Mesoproterozoic, and arc-continent collision in the Ordovician-Silurian (Fig. 4; Tang and Yan, 1993; Xiao et al., 2003; Eizenhöfer and Zhao, 2018). Both events are well documented geochronologically, which enabled us to place the development of REE mineralization in a temporal context. The emplacement of REE-rich carbonatites occurred in the Mesoproterozoic in response to rifting, which plays an essential role in global carbon cycling (Foley and Fischer, 2017). Following its separation from the Columbia supercontinent, the northern edge of NCC became a passive continental margin (Zhang and Zhao, 2016). The onset of southward (in present-day coordinates) subduction in the Ordovician was accompanied by the release of fluids carrying a metasedimentary isotopic signature, which triggered hydrothermal reworking and decarbonation of the H8 unit, and remobilization and concentration of REE to minable levels. The plate convergence lasted until ~410 Ma, but post-collisional magmatism was recorded for another 50 Ma (Ma et al., 2019), which explains the commonly reported Devonian ages of the Bayan Obo monazite (Song et al., 2018).

Conclusion

The C-Sr isotopic evolution of the mineralized H8 unit at Bayan Obo indicates that the precursor rock underwent dynamic recrystallization, metasomatic reworking and decarbonation, which resulted in volume loss and REE remobilization by fluids. The

driving forces for these secondary processes were plate convergence, subduction and the release of slab-derived fluids in the Silurian. The silica- and halogen-bearing, ^{87}Sr-rich fluids were responsible for the isotopic and trace-element re-equilibration of rock-forming dolomite, whereas the convergent tectonics determined the synclinal shape of the REE-rich H8 carbonatite and probably facilitated fluid ascent and circulation within it. These processes resulted in a wide range of complex textures and ore types. Although the size of the orebodies implies voluminous carbonatitic magmatism, our data support syn-deformational REE enrichment owing to decarbonation and volume loss without any need for external REE contributions.

Acknowledgements

We thank A.E. Williams-Jones, Charles Beard, Zengqian Hou and an anonymous referee for their constructive comments and suggestions to improve the manuscript. This research was financially supported by the National Natural Science Foundation of China (41825008) and Guangxi Natural Science Foundation (2020GXNSFGA297003). ARC acknowledges support from the Natural Sciences and Engineering Research Council (Canada).

REFERENCES

Aleinikoff, J.N., Schenck, W.S., Plank, M.O., Srogi, L., Fanning, C.M., Kamo, S.L., and Bosbyshell, H., 2006, Deciphering igneous and metamorphic events in high-grade rocks of the Wilmington Complex, Delaware: morphology, cathodoluminescence and backscattered electron zoning, and SHRIMP U-Pb geochronology of zircon and monazite: Geological Society of America Bulletin, v. 118, p. 39–64.

551 Bai, G., and Yuan, Z.X., 1985, Carbonatites and related mineral resources. Bulletin of
552 Institute of Mineral Deposits: Chinese Academy of Geological Sciences, v. 13, p.
553 107-140.
554 Balashov, V.N., and Yardley, B.W.D., 1998, Modelling metamorphic fluid flow with
555 reaction-compaction-peremability feedbacks: American Journal of Science, v.
556 298, p. 441-480.
557 Bau, M., and Dulski, P., 1995, Comparative study of yttrium and rare-earth element
558 behaviors in fluorine-rich hydrothermal fluids: Contributions to Mineralogy and
559 Petrology, v. 119, p. 213-223.
560 Chacko, T., Cole, D.R., and Horita, J., 2001, Equilibrium oxygen, hydrogen, and
561 carbon isotope fractionation factors applicable to geologic systems. In Stable
562 Isotope Geochemistry (eds. J. W. Valley and D. R. Cole): Reviews in Mineralogy
563 and Geochemistry, v. 43, p. 1-81.
564 Chacko, T., Mayeda, T., Clayton, R., and Goldsmith, J., 1991, Oxygen and carbon
565 fractionations between CO_2 and calcite: Geochimica et Cosmochimica Acta, v. 55,
566 p. 2867-2882.
567 Chakhmouradian, A.R., Reguir, E.P., Couëslan, C., and Yang, P., 2016, Calcite and
568 dolomite in intrusive carbonatites. II. Trace-element variations: Mineralogy and
569 Petrology, v. 110, p. 61-377.
570 Chakhmouradian, A.R., Reguir, E.P., Zaitsev, A.N., Couëslan, C., Xu, C., Kynicky, J.,
571 Mumin, A.H., and Yang, P., 2017, Apatite in carbonatitic rocks: Compositional
572 variation, zoning, element partitioning and petrogenetic significance: Lithos, v.
573 274-275, p. 188-213.
574 Chakhmouradian, A.R., and Wall, F., 2012, Rare earth elements: Minerals, mines,
575 magnets (and more): Elements, v. 8, p. 333-340.

576 Chao, E.C.T., Back, J.M., Minkin, J.A., and Ren, Y., 1992, Host-rock controlled
577 epigenetic, hydrothermal metasomatic origin of the Bayan Obo REE–Fe–Nb ore
578 deposit, Inner Mongolia, P.R.C: Applied Geochemistry, v. 7, p. 443-458.
579 Chao, E.C.T., Back, J.M., Minkin, J.A., Tatsumoto, M., Wang, J., Conrad, J.E., Makee,
580 E.H., Hou, Z., Meng, Q., and Huang, S., 1997, The sedimentary carbonate-hosted
581 giant Bayan Obo REE-Fe-Nb ore deposit of Inner Mongolia, China: A cornerstone
582 example for giant polymetallic ore deposits of hydrothermal original: U.S.
583 Geological Survey Bulletin 2143, 65 p.
584 Chebotarev, D.A., Veksler, I.V., Wohlgemuth-Ueberwasser, C., Doroshkevich, A.G
585 and Koch-Muller, M., 2019, Experimental study of trace element distribution
586 between calcite, fluorite and carbonatitic melt in the system $CaCO_3$+ CaF_2+
587 Na_2CO_3±Ca_3 $(PO_4)_2$ at 100 MPa: Contributions to Mineralogy and Petrology, v.
588 174(1), p. 1-13.
589 Chen, W., Liu, H.Y., Lu, J., Jiang, S.Y., Simonetti, A., Xu, C., and Zhang, W., 2020, The
590 formation of the ore-bearing dolomite marble from the giant Bayan Obo REE-Nb-
591 Fe deposit, Inner Mongolia: insights from micron-scale geochemical data:
592 Mineralium Deposita, v. 55, p. 131-146.
593 Deng, M., Xu, C., Song, W., Tang, H., Yun, L., Zhang, Q., Zhou, Y., Feng, M., and Wei,
594 C., 2017, REE mineralization in the Bayan Obo deposit, China: Evidence from
595 mineral paragenesis: Ore Geology Reviews, v. 91, p. 100-109.
596 Eizenhöfer, P.R., and Zhao, G., 2018, Solonker Suture in East Asia and its bearing on
597 the final closure of the eastern segment of the Palaeo-Asian Ocean: Earth-
598 Science Reviews, v. 186, p. 153-172.
599 Foley, S.F., and Fischer, T.P., 2017, An essential role for continental rifts and
600 lithosphere in the deep carbon cycle: Nature Geoscience, v. 10, p. 897-902.

601 Goodenough, K.M., Wall, F., and Merriman, D., 2018, The rare earth elements:
602 demand, global resources, and challenges for resourcing future generations.
603 Natural Resources Research, v. 27, p. 201–216.
604 Harlov, D.E., and Forster, H.J., 2003, Fluid-induced nucleation of (Y+REE)-phosphate
605 minerals within apatite: Nature and experiment. Part II. Fluorapatite: American
606 Mineralogist, v. 88, p. 1209-1229.
607 Harlov. D.E., Wirth, R., and Forster, H.J., 2005, An experimental study of dissolution-
608 reprecipitation in fluorapatite: fluid infiltration and the formation of monazite:
609 Contributions to Mineralogy and Petrology, v. 150, p. 268-286.
610 Hornig-Kjarsgaard, I., 1998, Rare earth elements in sovitic carbonatites and their
611 mineral phases: Journal of Petrology, v. 39, p. 2105-2121.
612 Hou, Z.Q., Liu, Y., Tian, S.H., Yang, Z.M., and Xie, Y. L., 2015, Formation of carbonatite
613 related giant rare-earth-element deposits by the recycling of marine sediments:
614 Scientific Reports, v. 5, p. 10231.
615 Hu, W.X., Kang, X., Cao, J., Wang, X.L., Fu, B. and Wu, H.G., 2018, Thermochemical
616 oxidation of methane induced by high-valence metal oxides in a sedimentary
617 basin: Nature Communications, v. 9, p. 5131.
618 Johnson, J.W., Oelkers, E.H., and Helgeson, H.C., 1992, SUPCRT92: a software
619 package for calculating the standard molal thermodynamic properties of minerals,
620 gases, aqueous species and reactions from 1 to 5000 bars and 0 to 1000 °C:
621 Computers & Geosciences, v. 18, p. 899–947.
622 Kusky, T.M., Polat, A., Windley, B.F., Burke, K.C., Dewey, J.F., Kidd, W.S.F.,
623 Maruyama, S., Wang, J.P., Deng, H., Wang, Z.S., Wang, C., Fu, D., Li, X.W., and
624 Peng, H.T., 2016, Insights into the tectonic evolution of the North China Craton
625 through comparative tectonic analysis: A record of outward growth of Precambrian

626 continents: Earth-Science Reviews, v. 162, p. 387-432.
627 Le Bas, M., Yang, X., Taylor, R., Spiro, B., Milton, J.A., and Peishan, Z., 2007, New
628 evidence from a calcite-dolomite carbonatite dyke for the magmatic origin of the
629 massive Bayan Obo ore-bearing dolomite marble, Inner Mongolia, China:
630 Mineralogy and Petrology, v. 90, p. 223–248.
631 Ling, M.X., Liu, Y.L., Williams, I.S., Teng, F.Z., Yang, X.Y., Ding, X., Wei, G.J., Xie, L.H.,
632 Deng, W.F., and Sun, W.D., 2013, Formation of the world's largest REE deposit
633 through protracted fluxing of carbonatite by subduction-derived fluids: Scientific
634 Reports, v. 3, p. 1776.
635 Ling, M.X., Zhang H., Li H., Liu Y.L., Liu, J., Li, L.Q., Li, C.Y., Yang, X.Y., Sun, W.D.,
636 2014, The Permian-Triassic granitoids in Bayan Obo, North China Craton: A
637 geochemical and geochronological study, Lithos, v. 190-191, p. 430-439.
638 Liu, Z.C., Wu, F.Y., Yang, Y.H., Yang, J.H., and Wilde, S.A., 2012, Neodymium
639 isotopic compositions of the standard monazites used in U-Th-Pb geochronology:
640 Chemical Geology, v. 334, p. 221-239.
641 Lowenstern, J.B., 2001, Carbon dioxide in magmas and implications for hydrothermal
642 systems: Mineralium Deposita, v. 36, p. 490-502.
643 Ludwig, K., 1994, ISOPLOT a Plotting and Regression Program for Radiogenic-
644 isotope Data: US Geological Survey, Open-file Report, Version 2.75, v. 91, p. 41-
645 45.
646 Ma, S., Wang, Z., Zhang, Y., and Sun, J., 2019, Bainaimiao arc as an exotic terrane
647 along the northern margin of the North China Craton: evidences from petrography,
648 zircon U-Pb dating, and geochemistry of the Early Devonian deposits: Tectonics,
649 v.38, p. 2606-2624.
650 Manning, C.E., 2004, The chemistry of subduction-zone fluids: Earth and Planetary

651 Science Letters, v. 223, p. 1-16.
652 Mcdonough, W.F., and Sun, S.S., 1995, The composition of the Earth: Chemical
653 Geology, v. 120, p. 223-253.
654 Plank, T., and Manning, C.E., 2019, Subducting carbon: Nature. v. 574, p. 343-352.
655 Pu, W., Gao, J.F., Zhao, K.D., Ling, H.F., and Jiang, S.Y., 2005, Separation method
656 of Rb-Sr, Sm-Nd using DCTA and HIBA: Journal of Nanjing University, v. 41, p.
657 445-450.
658 Ray, J., Ramesh, R., and Pande, K., 1999, Carbon isotopes in Kerguelen plume-
659 derived carbonatites: Evidence for recycled inorganic carbon: Earth and Planetary
660 Science Letters, v. 170, p. 205-214.
661 Ray, J.S., and Ramesh, R., 2000, Rayleigh fractionation of stable isotopes from a
662 multicomponent source: Geochimica et Cosmochimica Acta, v. 64, p. 299-306.
663 Sal'nikova, E.B., Yakovleva, S.Z., Nikiforov, A.V., Kotov, A.B., Yarmolyuk, V.V.,
664 Anisimova, I.V., Sugorakova, A.M., and Plotkina, Y.V., 2010, Bastnaesite: a
665 promising U-Pb geochronological tool: Doklady Earth Sciences, v. 430, p. 134-
666 136.
667 Scott, J.M., Smith, S.A.F., Tarling, M.S., le Roux, P.J., Harris, S., Hoffmann, J.E.,
668 Scherzer, S., and Tulley, C.J., 2019, Element and Sr–O isotope redistribution
669 across a plate boundary-scale crustal serpentinite mélange shear zone, and
670 implications for the slab-mantle interface: Earth and Planetary Science Letters, v.
671 522, p. 198-209.
672 Śliwiński, M.G., Kitajima, K., Kozdon, R., Spicuzza, M.J., Fournelle, J.H., Denny, A.,
673 and Valley, J.W., 2016a, Secondary ion mass spectrometry bias on isotope ratios
674 in dolomite–ankerite, Part I: $\delta^{18}O$ matrix effects: Geostandards and Geoanalytical
675 Research, v. 40, p. 157-172.

676 Śliwiński, M.G., Kitajima, K., Kozdon, R., Spicuzza, M.J., Fournelle, J.H., Denny, A.,
677 and Valley, J.W., 2016b, Secondary Ion Mass Spectrometry Bias on Isotope
678 Ratios in Dolomite–Ankerite, Part II: $\delta^{13}C$ Matrix Effects: Geostandards and
679 Geoanalytical Research, v. 40, p. 173-184.
680 Smith, M.P., 2007, Metasomatic silicate chemistry at the Bayan Obo Fe–REE–Nb
681 deposit, Inner Mongolia, China: Contrasting chemistry and evolution of fenitising
682 and mineralising fluids: Lithos, v. 93, p.126–148.
683 Smith, M.P., Campbell, L., and Kynicky, J., 2015, A review of the genesis of the world
684 class Bayan Obo Fe–REE–Nb deposits, Inner Mongolia, China: Multistage
685 processes and outstanding questions: Ore Geology Reviews, v. 64, p.459-476.
686 Smith, M.P., and Henderson, P., 2000, Preliminary fluid inclusion constraints on fluid
687 evolution in the Bayan Obo Fe–REE–Nb deposit, Inner Mongolia, China:
688 Economic Geology, v. 95, p. 1371-1388.
689 Smith, M.P., Moore, K., Kavecsanszki, D., Finch, A.A., Kynicky, J., Wall, F., 2016, From
690 mantle to critical zone: A review of large and giant sized deposits of the rare earth
691 elements: Geoscience Frontiers, v. 7, p. 315-334.
692 Song, W.L., Xu, C., Smith, M.P., Chakhmouradian, A.R., Brenna, M., Kynicky, J., Chen,
693 W., Yang, Y., Deng, M., and Tang, H., 2018, Genesis of the world's largest rare
694 earth element deposit, Bayan Obo, China: protracted mineralization evolution
695 over ~1 b.y.: Geology, v. 46, p. 323-326.
696 Song, W.L., Xu, C., Veksler, I.V., and Kynicky, J., 2016, Experimental study of REE,
697 Ba, Sr, Mo and W partitioning between carbonatitic melt and aqueous fluid with
698 implications for rare metal mineralization: Contributions to Mineralogy and
699 Petrology, v. 171, p. 1-12.
700 Sweeney, R.J., Green D.H. and Sie, S.H., 1992, Trace and minor element partitioning

701 between garnet and amphibole and carbonatitic melt: Earth and Planetary
702 Science Letters, v.113, p.1-14.
703 Tang, K.D., and Yan, Z., 1993, Regional metamorphism and tectonic evolution of the
704 Inner Mongolia suture zone: Journal of Metamorphic Geology, v. 11, p. 511–522.
705 Taylor, H.P., Frechen, J., and Degens, E.T., 1967, Oxygen and carbon isotope studies
706 of carbonatites from the Laacher See District, West Germany and the Alnö
707 District, Sweden: Geochimica et Cosmochimica Acta, v. 31, p. 407-430.
708 Tong, X., Liu, Y., Hu, Z., Chen, H., Zhou, L., Hu, Q., Xu, R., Deng, L., Chen, C., Yang,
709 L., and Gao, S., 2015, Accurate Determination of Sr Isotopic Compositions in
710 Clinopyroxene and Silicate Glasses by LA-MC-ICP-MS: Geostandards and
711 Geoanalytical Research, v. 40, p. 85-99.
712 Valley, J.W., 1986, Stable isotope geochemistry of metamorphic rocks: Reviews in
713 Mineralogy and Geochemistry, v. 16, p. 445–489.
714 Van Hoozen, C.J., Gysi, A.P., and Harlov, D.E., 2020, The solubility of monazite
715 ($LaPO_4$, $PrPO_4$, $NdPO_4$, and $EuPO_4$) endmembers in aqueous solutions from 100
716 to 250 ºC: Geochimica et Cosmochimica Acta, v. 280, p. 302-316.
717 Veizer, J., Clayton, R.N., and Hinton, R.W., 1992, Geochemistry of Precambrian
718 carbonates: IV. Early Paleoproterozoic (2.25 ± 0.25 Ga) seawater: Geochimica et
719 Cosmochimica Acta, v. 56, p. 875–885.
720 Verplanck, P.L., Mariano, A.N., and Mariano, A., 2016, Rare earth element ore geology
721 of carbonatites: Reviews in Economic Geology, v. 18, p. 5-32.
722 Wang, K.Y., Fan, H.R., Xie, Y.H., and Li, H.M., 2002, Zircon U-Pb dating of basement
723 gneisses in the super-large Bayan Obo REE-Fe-Nb deposit, Inner Mongolia:
724 Chinese Science Bulletin, v. 47, no.3, p. 243-246.
725 Weng, Z.H., Jowitt, S.M., Mudd, G.M., Haque, N., 2015, A detailed assessment of

726 global rare earth element resources: opportunities and challenges: Economic
727 Geology, v. 10, p. 1925-1952.
728 Wei, C.W., Xu, C., Chakhmouradian, A., Brenna, M., Kynicky, J., and Song, W., 2020,
729 Carbon–strontium isotope decoupling in carbonatites from Caotan (Qinling,
730 China): implications for the origin of calcite carbonatite in orogenic settings:
731 Journal of Petrology, v. 61, egaa024.
732 Xiao, W., Windley, B.F., Hao, J., and Zhai, M., 2003, Accretion leading to collision and
733 the Permian Solonker suture, Inner Mongolia, China: termination of the Central
734 Asian Orogenic Belt: Tectonics, v. 22, p. 1069.
735 Xie, Y., Hou, Z., Goldfarb, R. J., Guo, X., and Wang, L., 2016, Rare earth element
736 deposits in China: Reviews in Economic Geology, v. 18, p. 115-136.
737 Xie, Y.L., Verplanck, P., Hou, Z.Q., and Zhong, R.C., 2020, Rare Earth Element
738 Deposits in China: A Review and New Understandings: Economic Geology
739 Special Publication, no. 22, p. 509-552.
740 Xu, C., Campbell, I.H., Kynicky, J., Allen, C.M., Chen, Y., Huang, Z., and Qi, L., 2008,
741 Comparison of the Daluxiang and Maoniuping carbonatitic REE deposits with
742 Bayan Obo REE deposit, China: Lithos, v. 106, p. 12-24.
743 Xu, C., Chakhmouradian, A.R., Taylor, R., Kynicky, J., Li, W., Song, W., and Fletcher,
744 I., 2014, Origin of carbonatites in the South Qinling orogen: Implications for crustal
745 recycling and timing of collision between the South and North China Blocks:
746 Geochimica et Cosmochimica Acta, v. 143, p. 189–206.
747 Xu, C., Kynicky, J., Song, W.L., Tao, R., Lv, Z., Li, Y., Yang, Y., Zhang, L., and Fei, Y.,
748 2018, Cold deep subduction recorded by remnants of a Paleoproterozoic
749 carbonated slab: Nature Communications, v. 9, p. 2790.
750 Yang, K.F., Fan, H.R., Pirajno, F., and Li, X., 2019, The Bayan Obo (China) giant REE

accumulation conundrum elucidated by intense magmatic differentiation of carbonatite: Geology, v. 47, p. 1198-1202.

Yang, K.F., Fan, H.R., Santosh, M., Hu, F.F., and Wang, K.Y., 2011, Mesoproterozoic mafic and carbonatitic dikes from the northern margin of the North China Craton: implications for the final breakup of Columbia supercontinent: Tectonophysics, v. 498, p. 1-10.

Yang, Q.Y., and Santosh, M., 2015, Paleoproterozoic arc magmatism in the North China Craton: No Siderian global plate tectonic shutdown: Gondwana Research, v. 28, p. 82-105.

Yang, X.Y., Sun, W.D., Zhang, Y.X., and Zheng, Y.F., 2009, Geochemical constraints on the genesis of the Bayan Obo Fe-Nb-REE deposit in Inner Mongolia, China: Geochimica et Cosmochimica Acta, v. 73, p. 1417–1435.

Yang, Y.H., Sun, J.F., Xie, L.W., Fan, H.R., and Wu, F.Y., 2008, In situ Nd isotopic measurement of natural geological materials by LA-MC-ICPMS: Chinese Science Bulletin, v. 53, p. 1062-1070.

Yang, Y.H., Wu, F.Y., Li, R., Yang, J.H., Xie, L.W., Liu, Y., Zhang, Y.B., and Huang, C., 2014, In situ U-Pb dating of bastnaesite by LA-ICPMS: Journal of Analytical Atomic Spectrometry, v. 29, p. 1017–1023.

Yardley, B.W.D., 2005, Metal Concentrations in Crustal Fluids and Their Relationship to Ore Formation: Economic Geology, v. 100, p. 613-632.

Zhang, H.T., Zhang, H.F., Zou, D.Y., 2020, Comprehensive refertilization of the Archean–Paleoproterozoic lithospheric mantle beneath the northwestern North China Craton: Evidence from in situ Sr isotopes of the Siziwangqi peridotites: Lithos, v. 380–381, 105822.

Zhang, S.H., Zhao, Y., and Liu, Y., 2017, A precise zircon Th-Pb age of carbonatite sills

776 from the world's largest Bayan Obo deposit: Implications for timing and genesis
777 of REE-Nb mineralization: Precambrian Research, v. 291, p. 202-219.
778 Zhang, S.H., and Zhao, Y., 2016, Magmatic records of the Late Paleoproterozoic to
779 Neoproterozoic extensional and rifting events in the North China Craton: a
780 preliminary review. In Main Tectonic Events and Metallogeny of the North China
781 Craton (ed. M. Zhai), Springer Geology, p. 359-391.
782 Zhang, S.H., Zhao, Y., Ye, H., Liu, J.M., and Hu, Z.C., 2014, Origin and evolution of
783 the Bainaimiao arc belt: Implications for crustal growth in the southern Central
784 Asian orogenic belt: Geological Society of America Bulletin, v. 126, p. 1275-1300.
785 Zhang, Z.Q., Yuan, Z.X., Tang, S.H., Bai, G., and Wang, J.H., 2003, Age and
786 geochemistry of the Bayan Obo Ore Deposit. Geological Publishing House,
787 Beijing.
788 Zhu, X.K., Sun, J., 2012, Ore-forming epoch and episodes of ree mineralization in the
789 BayanObo ore deposit, Inner Mongolia: Acta Geoscientica Sinica, v. 33, p. 846-
790 856.
791 Zou, D.Y., Zhang, H.F., Zhang, X.Q., Zhang, H.T., Su B.X., 2020, Refertilization of
792 lithospheric mantle beneath the North China Craton in Mesozoic: Evidence from
793 in situ Sr isotopes of Fuxin peridotite: Lithos, v. 364-365, 105478.
794
795
796 **Figure captions**
797 Fig. 1. Simplified map showing the tectonic background of Bayan Obo (modified after
798 Xu et al., 2008; Zhang et al., 2014; Xie et al., 2020). The deposit is confined to the
799 northern margin of the NCC, close to the Paleozoic Bainaimiao arc and Ondor Sum
800 subduction complex, which were accreted to the NCC margin by ~410 Ma (Tang and

801 Yan, 1993; Xiao et al., 2003; Eizenhöfer and Zhao, 2018).

802 Fig. 2. Representative photomicrographs of mineralized dolomite carbonatites from
803 the H8 unit. (A) Dolomite (Dol) porphyroclasts fringed by small recrystallized grains,
804 fluorite (Fl) and (B) corresponding CL (cathode-luminescence) image; (C, D)
805 Photomicrograph and corresponding CL image of recrystallized dolomite. (E, F)
806 Photomicrograph and CL image of recrystallized dolomite showing non-luminescent
807 cores and orange rim, due to increase in Mn rim-wards.

808 Fig. 3 (A) Monazite (Mnz) occurring as sub- to euhedral crystals either in intimate
809 association with apatite (Ap), or (B) as monomineralic veinlets; note that the veinlets
810 yield much more consistent Th-Pb ages.

811 Fig. 4. Histogram of radiometric ages from the Bayan Obo deposit. Sm-Nd isochron
812 ages of whole-rock and REE ore samples, and carbonatite dikes are from Zhang et al.
813 (2017) and references therein; additional monazite data are from Song et al. (2018).
814 The tectonic setting during the shaded time periods (~ 400 Ma and 1300 Ma) was
815 related to subduction and rifting, respectively (Xiao et al., 2003; Eizenhöfer and Zhao,
816 2018).

817 Fig. 5. Compositional variation, expressed as (A) MgO vs. FeO,(B) MgO/(FeO+MnO)
818 vs. CaO/MgO, (C) Y/Ho vs. La/Ho and (D) La/Yb_{CN} vs. La/Nd_{CN} (chondrite-normalized;
819 Mcdonough and Sun, 1995), of dolomite grains from drill-core samples.

820 Fig. 6. (A, B) Trace-element abundances of porphyroclastic (precursor) and
821 recrystallized dolomite normalized to the chondrite data (Mcdonough and Sun, 1995).
822 Average porphyroclast and recrystallised dolomites are shown for comparison.

823 Fig. 7. (A) Isotopic variation, expressed as $\delta^{13}C_{VPDB}$ vs. $\delta^{18}O_{VSMOW}$ of dolomite grains
824 and whole-rock samples. Isotope fractionation trends at 400-500 ^{o}C are expressed in
825 terms of $\delta^{13}C_{VPDB}$ and $\delta^{18}O_{VSMOW}$ for Rayleigh-style dolomite decarbonation. The red

star represents the initial C-O isotopic composition, taken as the average $\delta^{18}O_{VSMOW}$ and $\delta^{13}C_{VPDB}$ values of the precursor dolomite porphyroclasts (13.51 ‰ and 0.72 ‰, respectively). Red triangles represent the final C-O isotopic compositions when the F(carbon) = 0.58 at 400-500 ^{o}C. Tick marks on the Rayleigh theoretical curves indicate fractionation intervals (5%). The typical C-O isotopic ranges of primary igneous carbonates (PIC; Taylor et al., 1967), 'normal' mantle (Ray et al., 1999), Paleoproterozoic sediments (Veizer et al., 1992) and sedimentary dolomite from Bayan Obo (Yang et al., 2009) are shown for comparison. (B) $^{87}Sr/^{86}Sr$ vs. $\delta^{13}C_{VPDB,}$ of dolomite grains and whole-rock samples from drill core. The Sr isotopic composition of Bayan Obo group sediment (Yang et al., 2019), Subduction-derived fluids (Scott et al., 2019), Silurian-Devonian (S-D) granitoids from the north margin of NCC (Zhang et al., 2014), and Archean-Paleoproterozoic (A-P) and Mesozoic (M) subcontinental lithosphere mantle (SCLM) of NCC (Zhang et al., 2020; Zou et al., 2020) are shown to illustrate the various potential sources of hydrothermal fluid in the sub-figure.

Fig. 8. Nd isotopic variation of REE minerals (monazite and bastnäsite) and whole-rocks from Bayan Obo. The $\varepsilon Nd_{(t)}$ values of drill-core samples were corrected to 1300 Ma (DC-1300) and 400 Ma (DC-400), and show a linear relationship congruent with the Nd isotope data for REE minerals. The data labelled "Monazite-Song" are from Song et al. (2018).

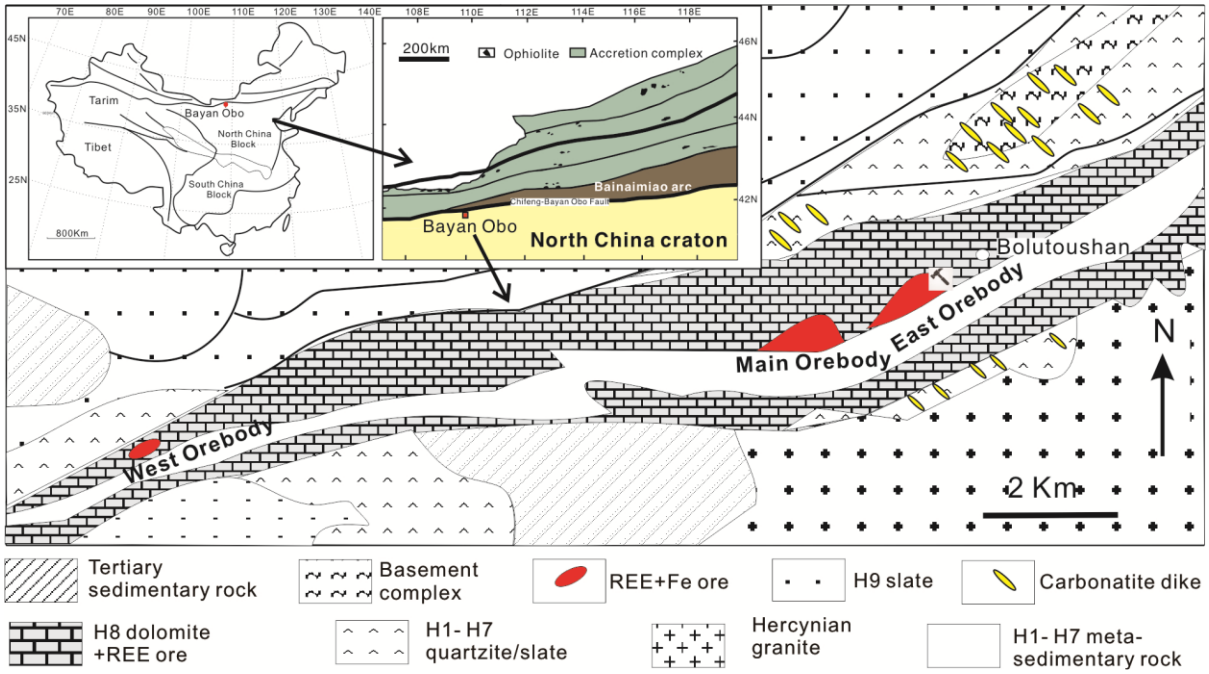

Fig. 1. Simplified map showing the tectonic background of Bayan Obo (modified after Xu et al., 2008; Zhang et al., 2014; Xie et al., 2020). The deposit is confined to the northern margin of the NCC, close to the Paleozoic Bainaimiao arc and Ondor Sum subduction complex, which were accreted to the NCC margin by ~410 Ma (Tang and Yan, 1993; Xiao et al., 2003; Eizenhöfer and Zhao, 2018).

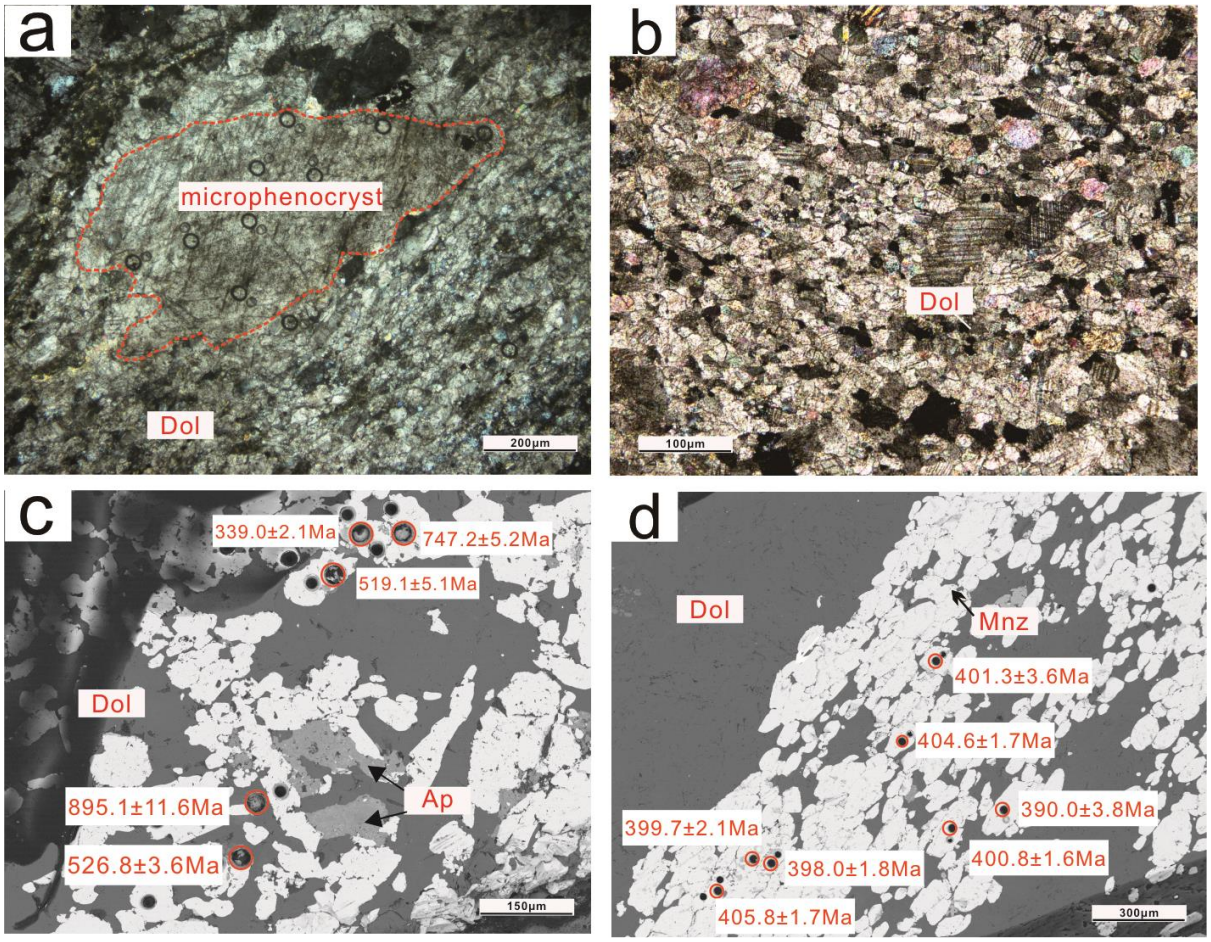

Fig. 2. Representative photomicrographs of mineralized dolomite carbonatites from the H8 unit. (A) Dolomite (Dol) porphyroclasts fringed by small recrystallized grains, fluorite (Fl) and (B) corresponding CL (cathode-luminescence) image; (C, D) Photomicrograph and corresponding CL image of recrystallized dolomite. (E, F) Photomicrograph and CL image of recrystallized dolomite showing non-luminescent cores and orange rim, due to increase in Mn rim-wards.

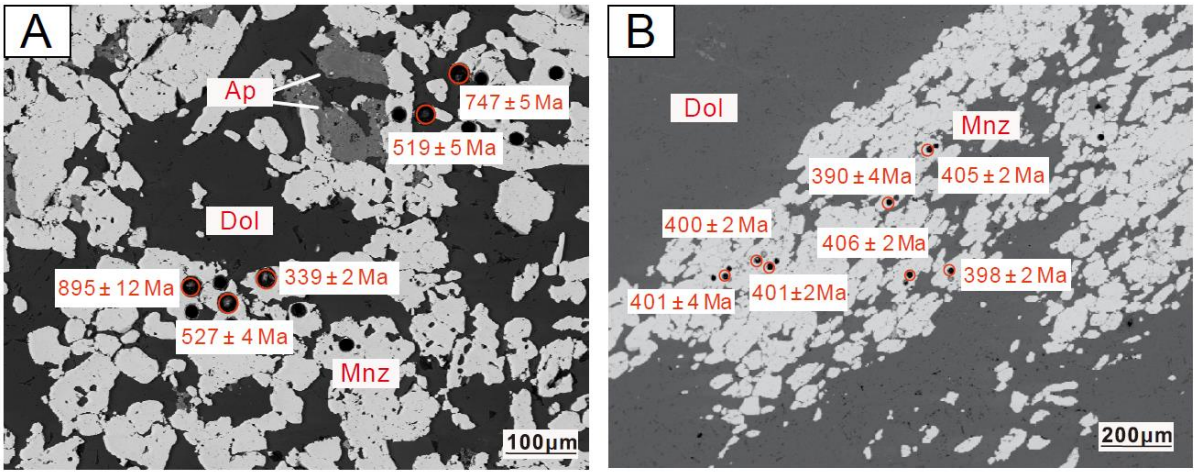

865

866 Fig. 3 (A) Monazite (Mnz) occurring as sub- to euhedral crystals either in intimate
867 association with apatite (Ap), or (B) as monomineralic veinlets; note that the veinlets
868 yield much more consistent Th-Pb ages.

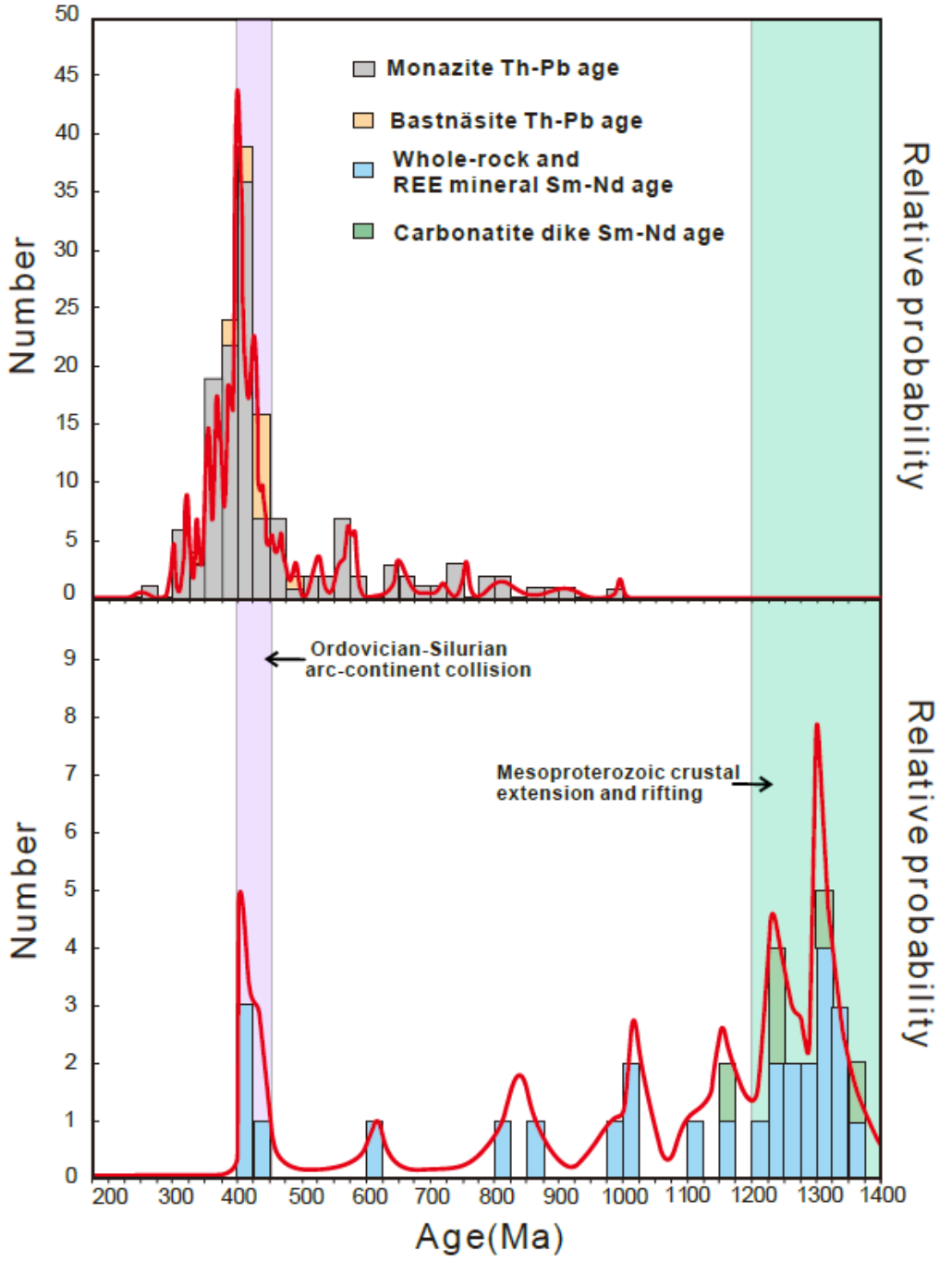

869

870 Fig. 4. Histogram of radiometric ages from the Bayan Obo deposit. Sm-Nd isochron
871 ages of whole-rock and REE ore samples, and carbonatite dikes are from Zhang et al.
872 (2017) and references therein; additional monazite data are from Song et al. (2018).
873 The tectonic setting during the shaded time periods (~ 400 Ma and 1300 Ma) was
874 related to subduction and rifting, respectively (Xiao et al., 2003; Eizenhöfer and Zhao,
875 2018).

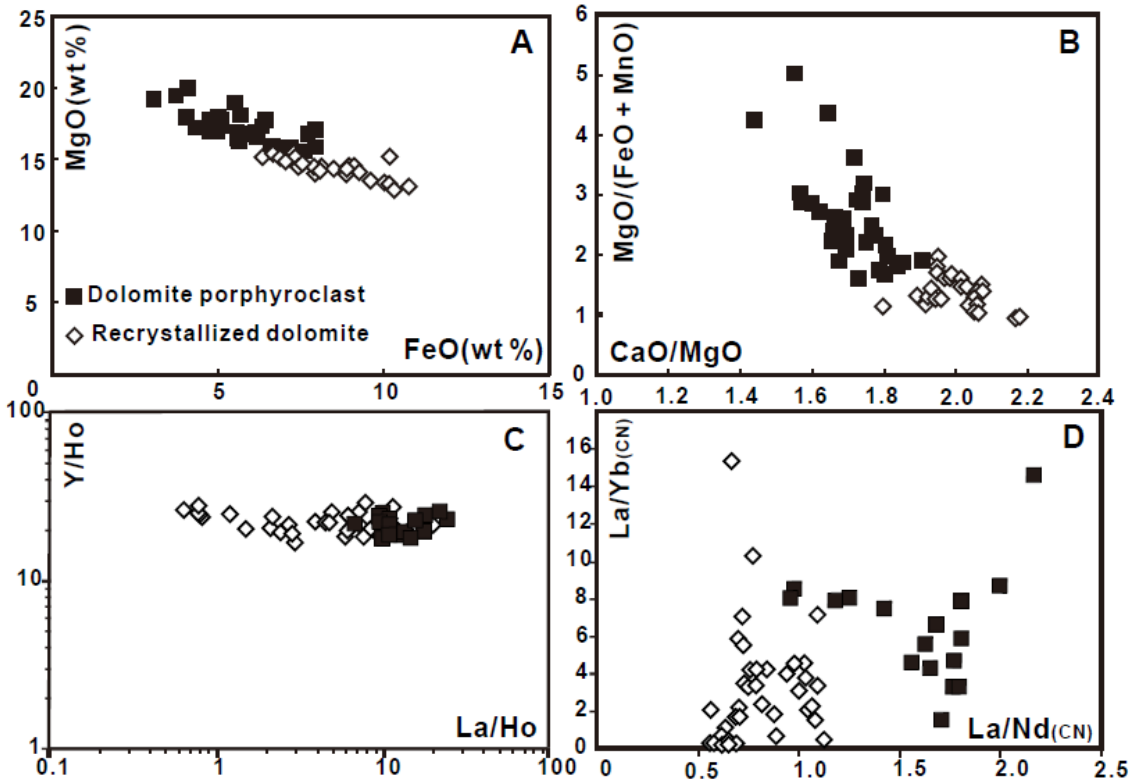

Fig. 5. Compositional variation, expressed as (A) MgO vs. FeO,(B) MgO/(FeO+MnO) vs. CaO/MgO, (C) Y/Ho vs. La/Ho and (D) La/Yb_{CN} vs. La/Nd_{CN} (chondrite-normalized; Mcdonough and Sun, 1995), of dolomite grains from drill-core samples.

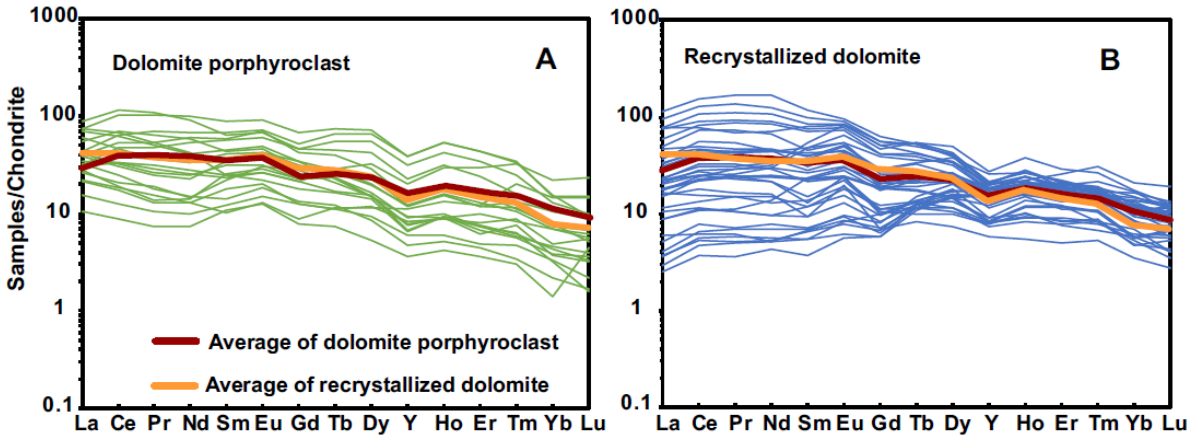

Fig. 6. (A, B) Trace-element abundances of porphyroclastic (precursor) and recrystallized dolomite normalized to the chondrite data (Mcdonough and Sun, 1995). Average porphyroclast and recrystallised dolomites are shown for comparison.

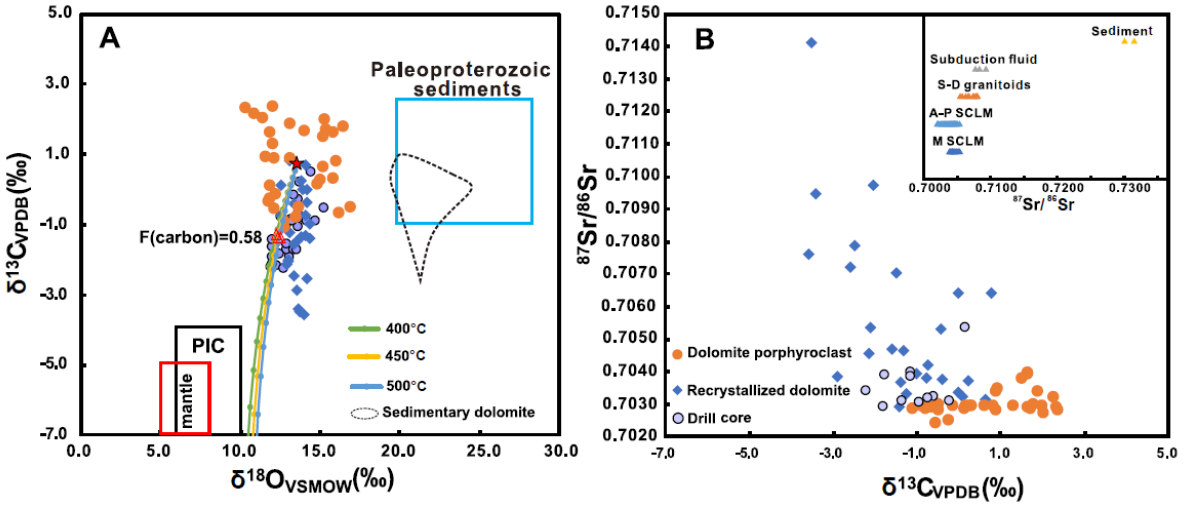

Fig. 7. (A) Isotopic variation, expressed as $\delta^{13}C_{VPDB}$ vs. $\delta^{18}O_{VSMOW}$ of dolomite grains and whole-rock samples. Isotope fractionation trends at 400-500 °C are expressed in terms of $\delta^{13}C_{VPDB}$ and $\delta^{18}O_{VSMOW}$ for Rayleigh-style dolomite decarbonation. The red star represents the initial C-O isotopic composition, taken as the average $\delta^{18}O_{VSMOW}$ and $\delta^{13}C_{VPDB}$ values of the precursor dolomite porphyroclasts (13.51 ‰ and 0.72 ‰, respectively). Red triangles represent the final C-O isotopic compositions when the F(carbon) = 0.58 at 400-500 °C. Tick marks on the Rayleigh theoretical curves indicate fractionation intervals (5%). The typical C-O isotopic ranges of primary igneous carbonates (PIC; Taylor et al., 1967), 'normal' mantle (Ray et al., 1999), Paleoproterozoic sediments (Veizer et al., 1992) and sedimentary dolomite from Bayan Obo (Yang et al., 2009) are shown for comparison. (B) $^{87}Sr/^{86}Sr$ vs. $\delta^{13}C_{VPDB}$, of dolomite grains and whole-rock samples from drill core. The Sr isotopic composition of Bayan Obo group sediment (Yang et al., 2019), Subduction-derived fluids (Scott et al., 2019), Silurian-Devonian (S-D) granitoids from the north margin of NCC (Zhang et al., 2014), and Archean-Paleoproterozoic (A-P) and Mesozoic (M) subcontinental lithosphere mantle (SCLM) of NCC (Zhang et al., 2020; Zou et al., 2020) are shown to illustrate the various potential sources of hydrothermal fluid in the sub-figure.

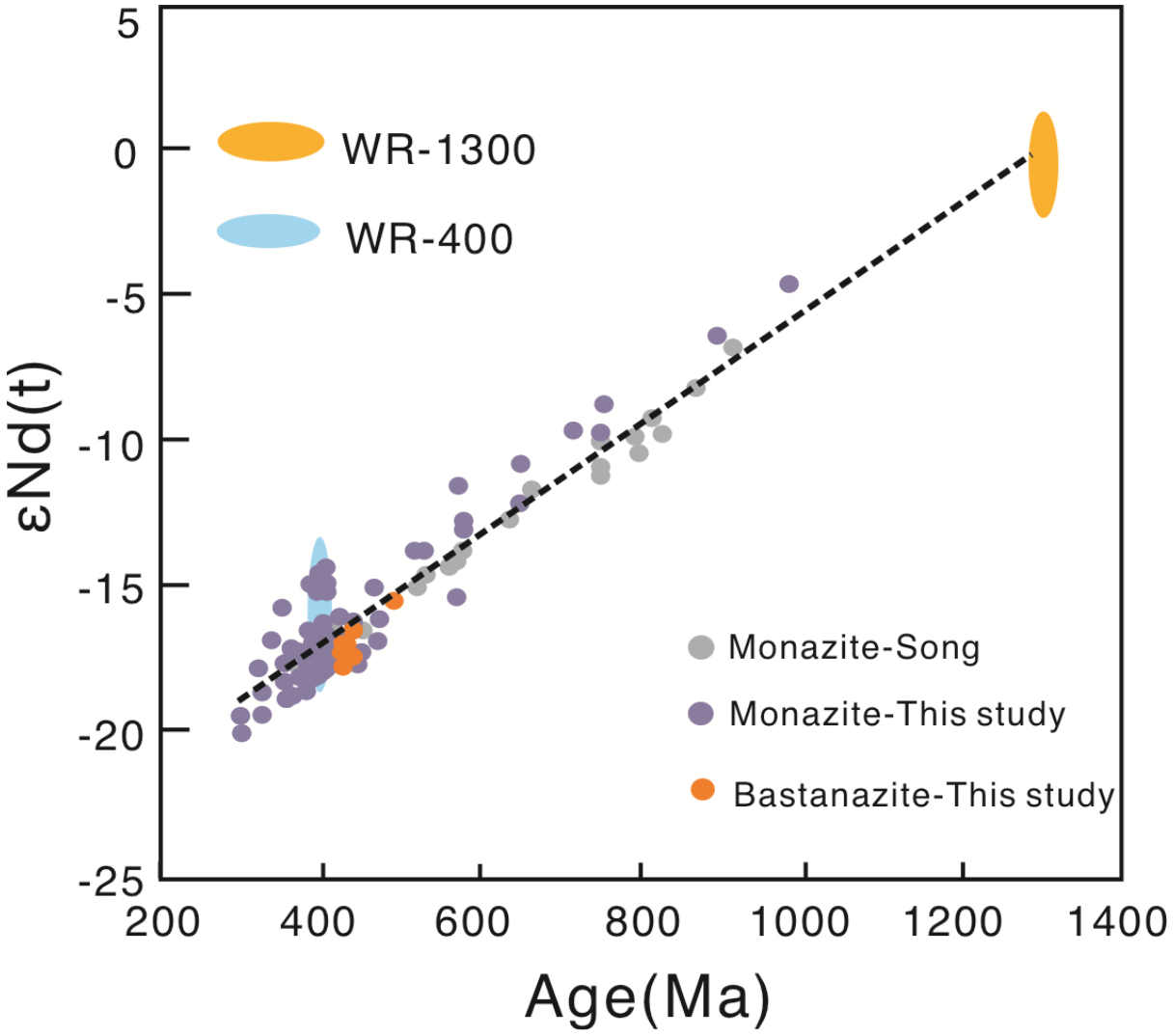

Fig. 8. Nd isotopic variation of REE minerals (monazite and bastnäsite) and whole-rocks from Bayan Obo. The $\varepsilon Nd_{(t)}$ values of drill-core samples were corrected to 1300 Ma (DC-1300) and 400 Ma (DC-400), and show a linear relationship congruent with the Nd isotope data for REE minerals. The data labelled “Monazite-Song” are from Song et al. (2018).